

# Extraction of a structural short-range order descriptor from nanobeam electron diffraction patterns using a transfer learning approach

Junjie Wu <sup>1</sup>, Timothy J. Rupert <sup>1,2,\*</sup>

<sup>1</sup> Department of Materials Science and Engineering, Johns Hopkins University, Baltimore, MD 21218, USA

<sup>2</sup> Hopkins Extreme Materials Institute, Johns Hopkins University, Baltimore, MD 21218, USA

\* Corresponding Author: [tim.rupert@jhu.edu](mailto:tim.rupert@jhu.edu)

## Abstract

Amorphous solids exhibit structural short-range order despite lacking long-range crystalline order, with this structural descriptor found to be important for determining mechanical properties. Nanobeam electron diffraction offers a potential route for experimental characterization of structural short-range order, yet efforts to date have been primarily qualitative in nature. In this work, machine learning approaches based on transfer learning are used to enable quantitative analysis of nanobeam electron diffraction data from amorphous solids. A ResNet-18 model is trained on virtual diffraction patterns taken from different locations within simulated metallic glasses and amorphous grain boundary complexions in the Cu-Zr alloy system that were created with hybrid molecular dynamics and Monte Carlo simulations. The disorder parameter is found to be a superior target structural descriptor compared to traditional Voronoi indices for this task. The model achieves a low validation mean absolute error across diffraction patterns corresponding to different interaction volumes, demonstrating excellent performance and potential transferability. Testing was performed using other simulated nanobeam electron diffraction data as well as experimental nanobeam electron diffraction patterns, showing that the model can

reliably capture spatial variations in local structural state. As a whole, this framework is able to overcome the challenges in the quantitative experimental characterization of structural short-range order, enabling improved characterization of amorphous solids and the exploration of structure-property relationships.

**Keywords:** short-range order, atomistic modeling, machine learning

## 1. Introduction

Amorphous solids are materials characterized by a lack of the long-range order typically seen in crystalline materials. Despite the absence of structural periodicity, amorphous solids exhibit unique properties due to their underlying local structural arrangement (e.g., see Ref. [1]), which can be referred to as structural short-range order (SSRO). One example of amorphous solids are metallic glasses, which have attracted significant research interest since they were first reported in 1960 [2]. Compared to their crystalline counterparts, metallic glasses are notable for their mechanical properties, such as high strength [3–8] and elastic limit [9–12]. At the same time, their practical applications are often restricted by their limited toughness [13,14], tensile ductility [15,16], and fatigue endurance [17,18]. The interplay between these properties and SSRO has been shown to be critical. First, SSRO is closely connected to the yielding behavior and shear band propagation in metallic glasses [19,20]. Atomic motifs such as full icosahedra are known to exhibit low potential energy, which enhances the strength and stability of metallic glasses [21]. Meanwhile, a higher concentration of densely packed icosahedra motifs suppresses atomic mobility, thereby reducing ductility [22]. Furthermore, the spatial heterogeneity of SSRO creates regions with varying atomic packing density, which can act either as crack barriers or as stress concentrators. In contrary to full icosahedra, geometrically unfavored motifs (GUMs), associated with higher potential energies and lower atomic packing fractions, can facilitate local atomic rearrangement under stress [23,24]. While such motifs contribute to a degree of plasticity, they also promote strain localization and propagation of shear bands, ultimately decreasing the toughness and fracture resistance of metallic glasses [25–27]. These relationships between SSRO and mechanical properties show the critical role of SSRO in the design of practical amorphous solids.

Amorphous grain boundary complexions, where amorphous intergranular films are formed through solute segregation between two crystals, are another example of a promising amorphous solid. For example, amorphous grain boundary complexions in nanocrystalline alloys have been shown to improve toughness and ductility by acting as damage tolerant interfacial features [28,29]. Mechanical testing of amorphous-crystalline nanocomposites demonstrates a similar simultaneous improvement of both strength and ductility [30,31]. Amorphous grain boundary complexions can act as strong dislocation sinks [32], reducing local stress concentration and resist crack nucleation at the interface [33]. Even subtle patterning of SSRO can be important for the mechanical behavior of amorphous complexions. For example, the asymmetry of SSRO between the amorphous-crystalline transition regions (ACTRs) on either side of the complexion were found to dramatically affect damage tolerance [34]. Similarly, amorphous grain boundary and interphase complexions were shown to provide superior radiation damage tolerance in Cu-Ta alloys compared to ordered boundaries, which was attributed to a heterogeneous distribution of excess atomic volume that facilitated more efficient defect recombination and annihilation [35].

While the importance of SSRO is clear, efforts to study such features are often restricted to atomistic simulations. Case in point, all of the literature examples discussed above relied on molecular dynamics (MD) simulations to probe the internal structure of amorphous solids. In an atomistic simulation, one can directly discuss SSRO because all atomic positions are known and local atomic packing can be directly observed and measured. In contrast, experimental study of SSRO remains challenging due to inherent difficulties in directly observing and quantifying nanoscale structural arrangements. High resolution transmission electron microscopy (TEM) has been used to analyze chemical short-range order of crystalline alloys [36–38], as the resolution of a TEM is fine enough to visualize sub-nanometer features, yet the lack of translational symmetry

in amorphous solids and the fact that TEM images are two-dimensional projections from a three-dimensional volume means that SSRO cannot be directly extracted from regular imaging. Complementary techniques such as atomic pair distribution function analysis can provide structural information on a global scale, yet cannot resolve local SSRO or its patterning that builds the overall amorphous network [39].

Nanobeam electron diffraction (NBED) is promising for measuring SSRO and uses a small, focused electron beam to probe local atomic arrangements. For example, Hirata et al. [40,41] identified geometric frustrated motifs in metallic glasses by comparing experimental NBED patterns with simulated diffraction data and finding qualitative similarities. As the beam size increases and large atomic volumes are probed, the diffraction pattern acquired gradually converges toward the halo rings seen in regular electron diffraction [40], meaning a small beam is required for probing SSRO. If information on the spatial distribution of local packing is sought, NBED patterns can be taken at every position across a two-dimensional grid in the sample through a technique known as four-dimensional scanning transmission electron microscopy (4D-STEM) [42]. NBED patterns and, by extension, 4D-STEM datasets are rich in information, yet are not easily converted into the same metrics one can take from atomistic simulations. Recent efforts have explored the use machine learning (ML) techniques to analyze NBED data from both crystalline and amorphous solids [43–46]. For example, Kang et al. [47] performed ML-assisted pair distribution function analysis to categorize a 4D-STEM dataset into local structural types. However, classification models do not distinguish between the different types of SSRO one can find in amorphous regions. Bruefach et al. [48] used unsupervised non-negative matrix factorization to extract features from raw diffraction patterns, which does not require prior knowledge but requires image calibration, yet the extracted features require additional analysis to

interpret. Consequently, there remains a need for a regression model capable of directly extracting a quantitative metric for SSRO from NBED patterns. Such a model would effectively bridge the gap between computational and experimental investigations of SSRO, and enable large-scale spatial mapping of structural order/disorder within amorphous solids.

In this work, an ML framework is designed to predict local SSRO from NBED patterns in the form of a local disorder parameter. By selecting a disorder parameter based on bond-orientation order [49], the model can capture the gradient of local SSRO in amorphous solids in terms of a metric that is commonly used in atomistic simulations. To ensure the robustness of our neural network in identifying diffraction patterns across varying disorder levels, the model is tested against a number of amorphous-crystalline configurations including amorphous grain boundary complexions and amorphous-crystalline composites. Additional validation is performed on experimental NBED patterns from the literature. As a whole, this study establishes a reliable approach for analyzing and interpreting complex diffraction patterns from NBED of amorphous solids.

## 2. Methods

### 2.1. *Computational models*

Hybrid molecular dynamics/Monte Carlo (MD/MC) simulations were performed using the Large-scale Atomic/Molecular Massively Parallel Simulator (LAMMPS) software [50] with an integration time step of 1 fs for all MD runs. Atomic interactions were modeled using the semi-empirical potential developed by Mendelev et al. [51] for the vitrification of Cu-Zr glasses. To ensure that the training data encompasses the full order-disorder spectrum from crystalline to fully amorphous, amorphous grain boundary complexions were simulated and used as the primary

source of training data. These complexions were selected due to their pronounced SSRO variations, which transition gradually from crystalline at the grain boundary interface to amorphous within the complexion interior [52]. The simulation starts with a Cu-Cu bicrystal, in which the two FCC grains are oriented in  $[110]$  and  $[00\bar{1}]$  along the X-direction, respectively, and both in  $[1\bar{1}0]$  along the Z-direction. The bicrystal was heated to and maintained at 1000 K for 100,000 steps using isothermal-isobaric (NPT) time integration, before being doped with 2 at.% Zr through hybrid MD/MC simulations using the variance constrained semi-grand canonical (VG-SGC) ensemble. MC swaps were attempted every 100 MD steps and the chemical potential was adjusted accordingly to control Zr concentration every 1,000 MD steps, with a total of 3,000,000 MD steps performed. The structure after minimization were visualized with OVITO software [53], as shown in Figures 1(a) and (b). Common neighbor analysis (CNA) was used to identify crystalline and defect regions. A zoomed view of the grain boundary region is shown in Figures 1(c) and (d), where a fully amorphous structure that is heavily doped with Zr is observed. In Figure 1(c), a few atoms appear yellow, signifying the identification of an icosahedral structure.

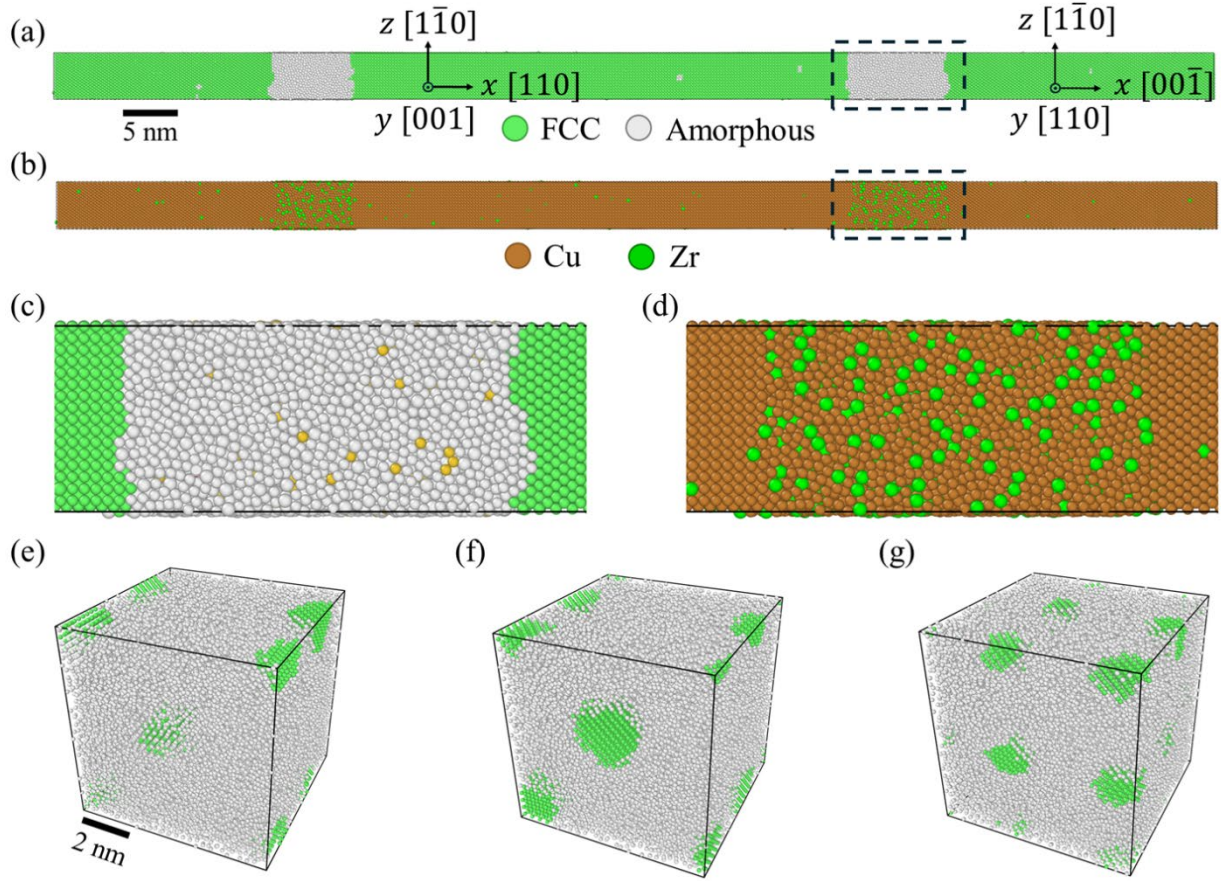


**Figure 1.** (a, b) Front view of the equilibrated amorphous grain boundary complexion sample. (c, d) Enlarged views of the amorphous grain boundary complexions formed between the crystalline Cu grains. Metallic glasses containing nanocrystals with radii of (e)  $4\times$  the lattice parameter of Cu and varied orientations, (f)  $4\times$  the lattice parameter of Cu and aligned orientations, and (g)  $3\times$  the lattice parameter of Cu and aligned orientations. (a, c, e-g) are colored by CNA while (b, d) are colored by particle type, with legends provided in the figure.

Amorphous-crystalline composite models were created to test the transferability of the model. Begin with bulk Cu crystals as the starting structure, spherical regions with radii of  $4\times$  or  $3\times$  the lattice parameter of Cu were kept frozen, while the remainder of the sample was doped by converting 36% of the atoms to Zr and melted by heating the system to 2000 K. The system was held at this temperature and everything except the small frozen crystalline regions became liquid. The samples were then cooled to 700 K with a quenching rate of 100 K/ns. Next, the nanocrystals

were released from their frozen state, and the system was further equilibrated at 700 K for 2 ns. Finally, the entire system was cooled to 300 K at the same rate with a quenching rate of 100 K/ns. An additional sample was created following the same procedure, with the nanocrystals rotated with respect to one another. The final amorphous-crystalline nanocomposite samples are shown in Figures 1(e)-(g), where small crystalline regions (green) are seen scattered throughout an amorphous matrix (white).

## 2.2. *SSRO analysis*

The quenched system was analyzed with multiple techniques to evaluate SSRO. One of these is Voronoi tessellation, which segments the material into Voronoi polyhedra that are defined as the region in space closer to that atom than any other and are bounded by planes equidistant from neighboring atoms. This technique characterizes atomic environments by assigning each polyhedron an index to describe each Voronoi polyhedron, most typically of the form  $\langle n_3, n_4, n_5, n_6 \rangle$  where  $n_i$  represents the number of faces in the polyhedron with  $i$  edges [54]. These indices allow for identification and classification of common motifs. For example, when Cu is the central atom in our Cu-Zr system, the densely packed and fully ordered face-centered cubic (FCC) motifs correspond to Voronoi index of  $\langle 0, 12, 0, 0 \rangle$  which represents 12 four-edged faces. Alternatively, the icosahedral motifs that are important for certain properties and are low energy states have a Voronoi index of  $\langle 0, 0, 12, 0 \rangle$ , with 12 five-edged faces. In some cases, nearby Voronoi indices can signal similar shapes, such as when  $\langle 0, 10, 2, 0 \rangle$  and  $\langle 0, 2, 10, 0 \rangle$  resemble distorted FCC and distorted icosahedra motifs, respectively. It is important to note that this is not always the case and there is no generally rule that enables comparison between different

Voronoi motifs only based on their indices. To mitigate the impact of small faces on the validity of Voronoi index, an edge length threshold of 0.6 Å was applied here.

Local SSRO can also be characterized by descriptors calculated from bond-orientation order [49,55,56]. Many atomistic studies of grain boundary structure employ a disorder parameter,  $d_i$ , which provides a measure of where a structure falls on the order-disorder spectrum. First, a normalized complex vector consisting of components  $\hat{Y}_{lm} = \bar{Y}_{lm}/|\bar{Y}_{lm}|$  for each atom is computed, where  $\bar{Y}_{lm}$  is the average of the spherical harmonics  $Y_{lm}$ . Next, the degree of similarity between an atom  $i$  and its neighbors is given by:

$$s_{ij} = \sum_{m=-l}^l \hat{Y}_{lm}(i) \hat{Y}_{lm}^*(j) \quad (1)$$

The disorder parameter of atom  $i$  is then given by:

$$d_i = 1 - \frac{|s_{ij}|}{N_i} \quad (2)$$

where  $N_i$  denotes the number of neighboring atoms.  $N_i$  was chosen to be 12 in this work because bulk Cu and Zr both have this coordination number in their crystalline states. The disorder parameter measures the average dissimilarity between an atom and its neighbors, such that a value of 0 corresponds to crystalline phases and a value of 1 indicates pure liquid that is fully disordered [56]. To provide comparison, a reduced bond-orientational order was also computed as follows:

$$1 - Q_l = 1 - \sqrt{\frac{4\pi}{2l+1} \sum_{m=-l}^l \bar{Y}_{lm} \bar{Y}_{lm}^*} \quad (3)$$

In this case,  $l$  is set to 6. This reduced form is for the convenience of assessing the degree of disorder in a manner analogous to the disorder parameter.

### 2.3. Virtual diffraction and ML analysis

Virtual diffraction simulations were performed using the *compute saed* command in LAMMPS. Diffraction regions were sampled with one of the four types: (1) 1-layer atomic cluster, which consisting of a center atom and its neighbors, (2) 2-layer atomic cluster, where nearest neighbors of the target atom's nearest neighbors are also included, (3) cylinder, and (4) ellipsoid. Similar to a 4D-STEM scan, diffraction regions were sampled from different positions in the amorphous grain boundary complexion and nearby crystalline regions. For the 1-layer and 2-layer Voronoi clusters, complete spherical virtual diffraction meshes were computed, from which diffraction patterns were sampled by slicing along different zone axes. For the cylinder and ellipsoid regions, diffraction meshes of incident electron beam with zone axis parallel to the shape's major axis were computed and the diffraction patterns were then obtained by slicing the diffraction mesh perpendicular to the zone axis.

To expedite the training process of a highly accurate model, transfer learning technique was used. A pre-trained ResNet-18 [57], capable of classifying 1000 classes on ImageNet, was further trained for 400 epochs using the Adam [58] optimizer with a learning rate of 0.001 and mean absolute error (MAE) loss. A learning rate scheduler was applied to reduce the learning rate by half on plateau. Additional details and discussion of model will be presented below in the Results and Discussion section.

### 3. Results and Discussion

To begin, it is important to establish an understanding of the ground truth for SSRO within the modeled materials. Here, an amorphous grain boundary complexion is used as a representative example, since it contains both ordered and disordered regions. Figure 2 shows the spatial variation of the three SSRO descriptors across the complexion sample: (1) the distribution of representative Voronoi polyhedra, (2) the disorder parameter  $d_i$ , and (3) the reduced bond-orientational order  $1 - Q_6$ . Starting with the Voronoi polyhedra, which have been extensively used in the computational study of SSRO in various types of amorphous solids [19,59–63], Cu is chosen as the central atom since it is the dominant atom present while the  $< 0, 10, 2, 0 >$  and  $< 0, 2, 10, 0 >$  motifs are specifically shown since they are close to the well-defined FCC and icosahedral structures. The  $< 0, 10, 2, 0 >$  polyhedra predominantly appear as two peaks near the ACTRs, while the  $< 0, 2, 10, 0 >$  polyhedra are present only in the complexion interior. Figure 3 shows a more detailed description of the amorphous complexion with the eight most frequent non-FCC Voronoi motifs shown. The ACTR is primarily filled with the  $< 0, 10, 2, 0 >$  and  $< 0, 8, 4, 0 >$  polyhedra, dominating the regions where X-position ranges from around 185 to 193 Å and from 277 to 286 Å. In contrast, these motifs fall to very low densities in the complexion interior, where the other six visualized motifs dominate.

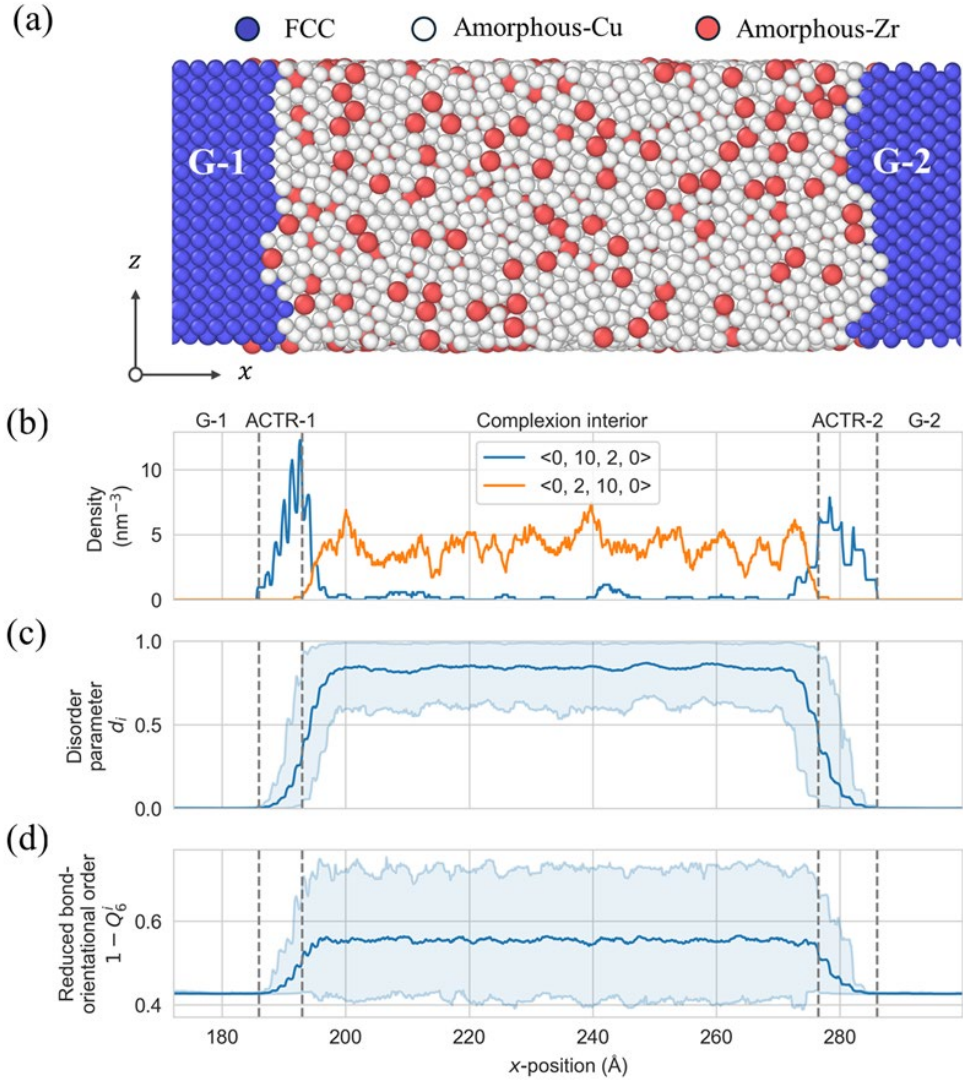


**Figure 2. (a) Visualization of an amorphous grain boundary complexion in Cu-Zr. Distributions of the (b)  $\langle 0, 10, 2, 0 \rangle$  and  $\langle 0, 2, 10, 0 \rangle$  Voronoi polyhedra with Cu as the central atom, (c) disorder parameter  $d_i$ , and (d) reduced bond-orientational order  $1 - Q_6'$ . For (c) and (d), the center line, upper bound and lower bound denote the mean, 95th percentile, and 5th percentile values, respectively. The two grains are denoted G-1 and G-2, while the beginning and end of the ACTRs were chosen based on the positions where  $\langle 0, 10, 2, 0 \rangle$  and  $\langle 0, 2, 10, 0 \rangle$  polyhedra emerge, respectively.**

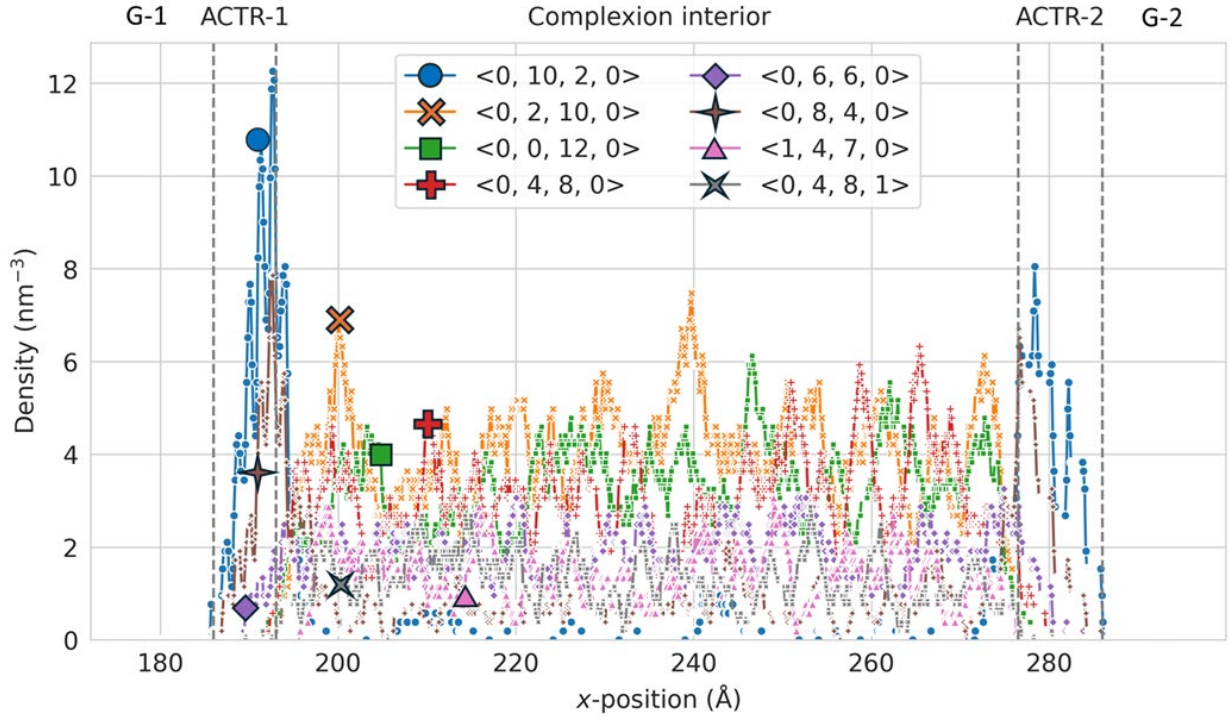


**Figure 3. Spatial density variations of the eight most frequent Voronoi motifs in the model (excluding FCC motifs) with Cu as the center atom along the thickness direction in the amorphous grain boundary complexion.**

Figure 2(b) and Figure 3 show that Voronoi polyhedra can be used to identify the ACTR and complexion interior, yet the use of Voronoi indices as an overall SSRO descriptor presents several challenges. First, a cluster of atoms can contain a number of distinct Voronoi indices due to the heterogeneity of local atomic arrangements in amorphous solids, meaning the assignment of a single value to the region is not possible. Second, there are a large number of Voronoi indices. Figure 3 shows the spatial density of the eight most frequent Voronoi polyhedra excluding FCC, yet this only represents 27.53% of the Cu atoms in the complexion. A total of 816 different motifs would need to be considered to fully describe the SSRO of the Cu atoms, making direct prediction of Voronoi indices impractical. If one were to include the Zr atoms, which have different baseline descriptions, even more motifs would need to be treated. This also highlights a common limitation of computational studies that is often overlooked. If Voronoi index is used to describe the local

structure in an atomistic modeling study, the analysis often is limited to one atomic species because this enables an easy comparison. In an atomic scale model where one can simple ignore other species, this works, yet experimental signals will include all atoms. Classification models are possible yet lack the ability to describe specific structural states. For example, Kang et al. [47] used ML-assisted 4D-STEM to map SSRO in an  $\text{Fe}_{85.2}\text{Si}_{0.5}\text{B}_{9.5}\text{P}_4\text{Cu}_{0.8}$  glass into solid-like and liquid-like regions. However, amorphous regions with different degree of disorder are indistinguishable with such a scheme, meaning there is an oversimplification of atomic environments resulting in a loss of data granularity. Although it is possible to categorize Voronoi polyhedra into finer groups, such as the twelve building-block groups proposed by Weeks and Flores [64] or ordered and disordered classifications introduced by Garg and Rupert [65], details are still suppressed and an incomplete picture of SSRO would result. In addition, in the context of mapping diffraction patterns to SSRO, the orientation dependence of local SSRO creates instability in regression models, as minor changes in diffraction patterns can result from a drastic change in Voronoi index. For example, a  $\langle 0, 10, 2, 0 \rangle$  motif is structurally close to a  $\langle 0, 12, 0, 0 \rangle$  FCC motif, yet their diffraction pattern can differ significantly due to geometric frustration of the atoms. Similarly, a motif may exhibit different symmetries depending on the viewing orientation [41].

To overcome these limitations, the disorder parameter  $d_i$  (Figure 2(c)) and the reduced bond-orientational order parameter  $1 - Q_6$  (Figure 2(d)) were explored as possible candidates for SSRO descriptor within an ML analysis environment. First and foremost, a successful descriptor must identify the key structural signatures of interest. The moving average (center line) of both  $d_i$  and  $1 - Q_6$  show similar trends across the amorphous grain boundary complexion. They begin at a nearly constant value within FCC regions, increase monotonically across the ACTR, and

eventually reach a plateau within the complexion interior. However, the reduced bond-orientational order parameter ranges from approximately 0.40 to 0.75 in the complexion interior. Given that the reduced bond-orientational order parameter for FCC is 0.42, this descriptor provides a limited ability to distinguish between crystalline and amorphous regions, let alone comment on differences in SSRO. In contrast, the lowest data points from  $d_i$  stay above 0.6 in the complexion interior, significantly differing from both the ACTR and the FCC grain interior. Disorder parameter thus provides an interpretable metric of disorder, ranging from 0 in the crystal to a mean value near 1 in the complexion interior. Additionally, for larger diffraction volumes, the gradients exhibited in the moving average  $d_i$  suggest that the average  $d_i$  of atomic clusters are still distinguishable between each other. It is important to note that the size of atomic cluster needs to be small enough to not wash out the signal, which will be discussed later as different diffraction volumes are probed.

Finally, for the disorder parameter to be a promising candidate as an SSRO descriptor, it must be able to distinguish the features of interest in an amorphous solid. As mentioned earlier, previous studies have highlighted the importance of certain groups of Voronoi motifs on mechanical properties. Figure 4(a) shows the distribution of  $d_i$  for different Voronoi polyhedra categorizations: FCC, ordered, intermediate, and disordered. Here, the term “ordered” refers to motifs with  $n_4 \geq 8$ ,  $n_5 \leq 4$  and  $n_6 = 0$ , including  $< 0, 10, 2, 0 >$  and  $< 0, 8, 4, 0 >$  plus a few others, based on their (1) geometric similarity with FCC motifs ( $< 0, 12, 0, 0 >$  and (2) spatial dominance in the ACTR [52]. Similarly, “disordered” motifs refer to Voronoi polyhedra with  $n_4 \leq 2$ ,  $n_5 \geq 10$  and  $n_6 = 0$ , such as  $< 0, 0, 12, 0 >$  (icosahedral),  $< 0, 2, 10, 0 >$  (distorted-icosahedron) and a few others that exist mostly in the disordered complexion interior. Starting from the FCC motifs, 98.9% of them have a  $d_i$  lower than 0.01. The outliers are located near the

amorphous-crystalline interface, as their  $d_i$  shows the contextual information of their atomic environment that is missing in Voronoi analysis. While the atoms are part of the crystal, the region nearby is distorted. The median  $d_i$  of ordered and disordered motifs are 0.290 and 0.915, respectively, clearly separating the two populations. By minimizing the total error rate in classifying ordered and disordered motifs, a threshold value of 0.768 works as an effective boundary condition for distinguishing ordered and disordered motifs. Although the  $d_i$  for ordered motifs exists over a broader range, 91.38% of the ordered motifs have a  $d_i$  lower than 0.768, while 96.43% of the disordered motifs have a  $d_i$  higher than 0.768. The remaining, non-FCC polyhedra are referred to as “intermediate” motifs, which fill up the remaining space in amorphous structures. Among these are the motifs previously referred to as GUMs, which are geometrically unfavored for space tiling and energetically less stable [66,67]. There are of course hundreds of others that have no special name. The disorder parameter value for the intermediate structures, being neither completely ordered nor disordered, falls at intermediate values between those extreme yet important cases.

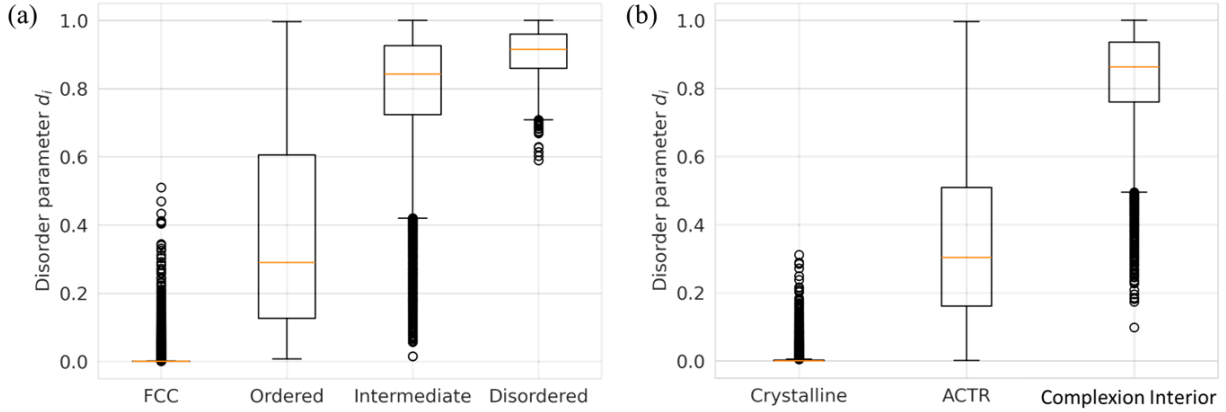


**Figure 4.** The distribution of the disorder parameter  $d_i$  according to (a) prior classification schemes from [65] and (b) the location within the amorphous grain boundary complexion. The orange center line, boxes and whiskers represent the median, first quartile to third quartile range, and 1.5 interquartile range, respectively.

The complexions themselves provide another way to further examine the rigor of the disorder parameter, as the ACTR and complexion interiors are noticeably different. Figure 4(b) presents the  $d_i$  distribution in the crystalline grains, ACTR, and complexion interior. While crystalline regions were identified directly by CNA, amorphous regions whose distance away from the crystalline-amorphous interface is less than 5 Å were identified as ACTR while the rest were identified as the complexion interior. A distinct signal in  $d_i$  can be found between the ACTR and the complexion interior, as their median values are 0.304 and 0.863, respectively. Using the threshold of 0.768 discussed in the previous paragraph, 92.2% of polyhedra in the ACTR have a  $d_i$  lower than the threshold and 73.5% of polyhedra in the complexion interior have a  $d_i$  higher than the threshold. Some level of overlap here is to be expected, as a number of SSRO motifs are observed both in the ACTR and complexion interior. In other words, these regions are different yet do have features in common. Both the comparison of ordered and disordered packing motifs as well as the comparison of different interfacial environments show that the disorder parameter is capable of characterizing important variations in SSRO.

To build a model capable of predicting disorder parameter, the framework shown in Figure 5 was trained with virtual diffraction patterns from different positions across the amorphous grain boundary complexion. ResNet-18, a deep convolution neural network (CNN) featuring residual connections, was chosen in this task to because of its generalizability and fast convergence [57]. To accelerate model training, each iteration was initialized with weights pre-trained with ImageNet dataset and then these models continued being trained with virtual diffraction dataset. Each dataset consisted of virtual diffraction patterns with a size of 133×133 pixels that were computed from regions of three types of geometries (crystalline, ACTR, and complexion interior). The data was split into training and validation sets of 80% and 20%, respectively.

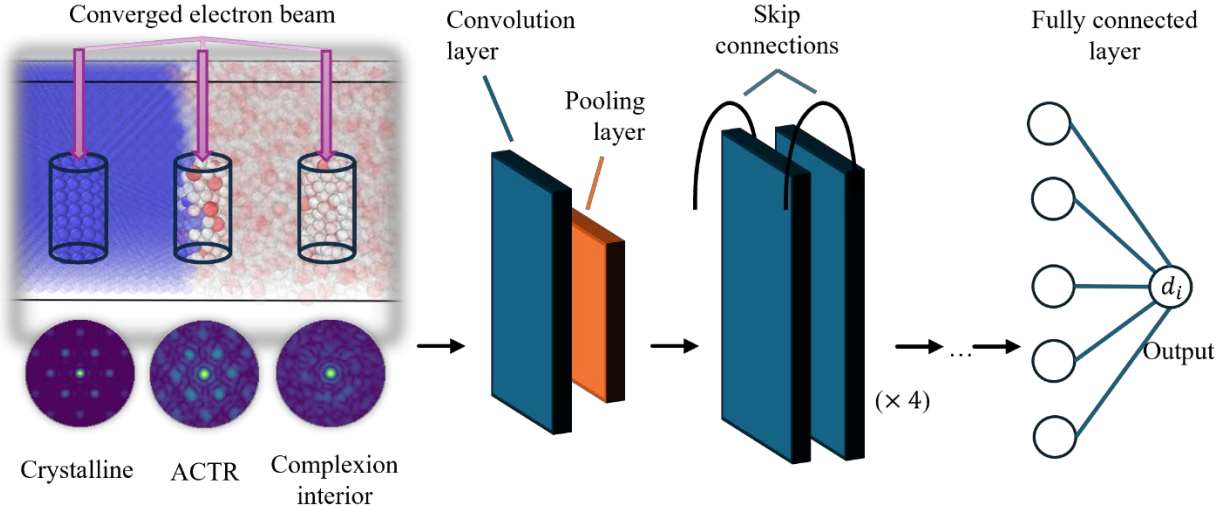


**Figure 5. Schematic illustration of machine learning analysis of an NBED dataset. Virtual diffraction patterns of regions sampled from different positions within the amorphous grain boundary complexion sample are used as inputs into a ResNet-18 model consisting of an initial convolution layer and pooling layer, 4 residual blocks with skip connections, and a fully connected output layer that transform high-dimensional data into predictions for disorder parameter  $d_i$ .**

To ensure the generalizability of the model and examine the limits on input diffraction patterns, it is necessary to connect the simulation volumes used to create the virtual diffraction patterns. Figure 6 shows the performance of models trained with different effective diffraction volumes. In general, variations of the models trained with cylindrical and ellipsoidal volumes have superior performance (Figure 6(b-d)) than models trained with the 1-layer atomic clusters, in which effective diffraction volume consists only of the center atom and its nearest neighbors or its Voronoi volume (Figure 6(a)). This is a positive outcome, as real NBED experiments will obtain a signal from more than a single atomic environment, with the cylindrical and ellipsoidal shapes representing simple models of typical electron beam interaction volumes. The model for NBED of 1-layer atomic clusters is not physically realistic. Both cylindrical and ellipsoidal model perform well, with the model trained on cylindrical diffraction volumes slightly outperforming the one trained on ellipsoidal regions. For more disorder regions, especially data points with a

computed  $d_i$  of larger than 0.7 that largely reside in the complexion interior, all models exhibit larger but acceptable error. This could be attributed to the more complex symmetries of the disordered configurations, making them harder to be distinguished between each other [41]. Notably, the disordered regions mostly reside in the complexion interior and the deviations from predicted values are small, meaning the model can still tell the different regions of the amorphous complexion apart. Due to the better performance and more realistic shape, only models trained with data sampled from cylinder regions will be discussed for the rest of the manuscript.

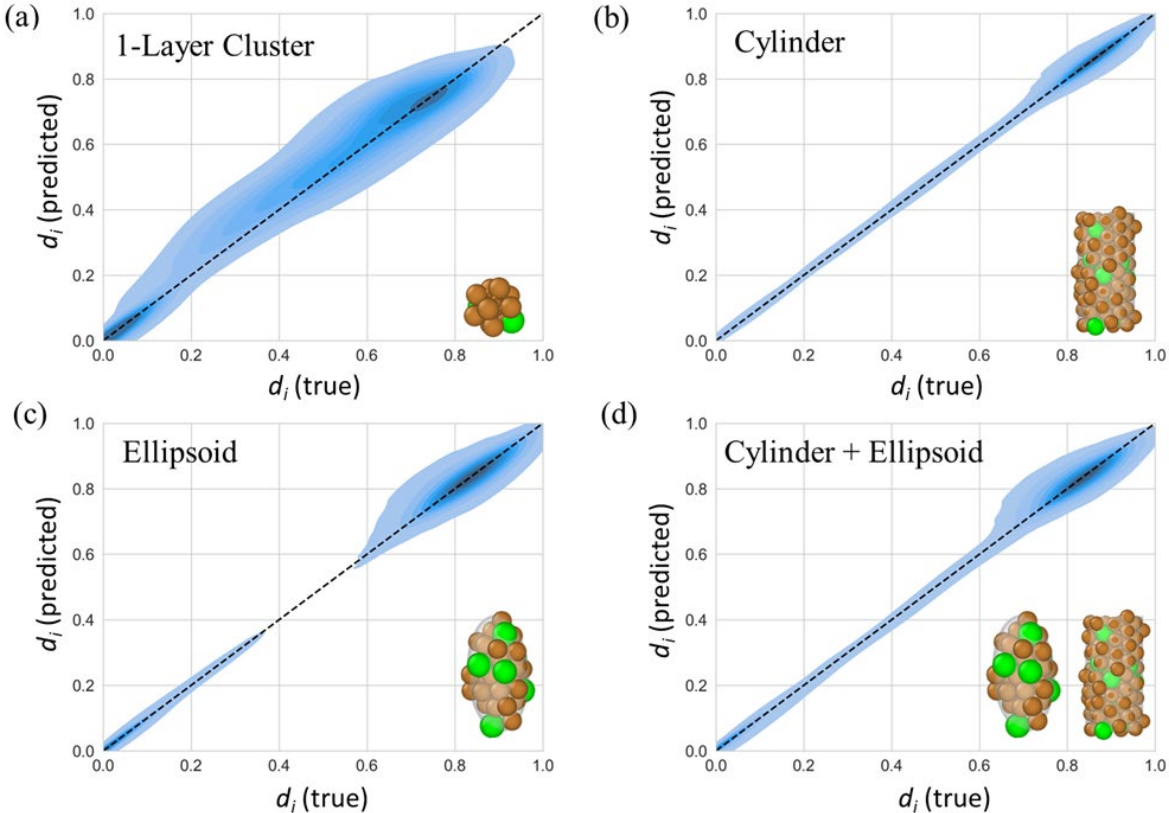


**Figure 6. Validation accuracy of ML model trained with virtual diffraction patterns from (a) 1-layer clusters, (b) cylinders, (c) ellipsoids, and (d) both cylinders and ellipsoids. The closer data points are to the diagonal black dash line, which denotes where predictions perfectly match with true values, the higher the prediction accuracy is.**

To further investigate the impact of effective diffraction volume geometry, this time in terms of with experimental conditions such as beam size and sample thickness, the performance of the model trained with cylinders of different dimensions is plotted in Figure 7. A base CNN model with three convolutional layer and two fully connected output layer was used for comparison between training with mean absolute error in Figure 7(a) and mean squared error in Figure 7(b). Another model that used pretrained Resnet-18 and then trained with mean absolute error is shown in Figure 7(c). For all of the models, cylinders of 25 Å height and 5 Å radius have the lowest loss, while a height of 40 Å and a radius of 5 Å yields the highest loss. It is worth noting that while loss appears to go down as height is further increased above 40 Å, this is primarily due to the diffraction patterns containing information from a larger volumes and therefore less information about SSRO. In other words, the correct answer is found, yet the information gained is less useful. On the other hand, smaller volumes are not always better. For example, the combination of 10 Å height and 5 Å radius has worse performance than a diffraction volume with a larger radius. One needs to capture enough atoms to obtain meaningful information on the SSRO as well. This is consistent with experimental reports of NBED patterns with varying beam sizes. Small beam sizes were found to be difficult to interpret due to orientational dependence and spatial variation, while large beam size results in trivial halo rings [40].

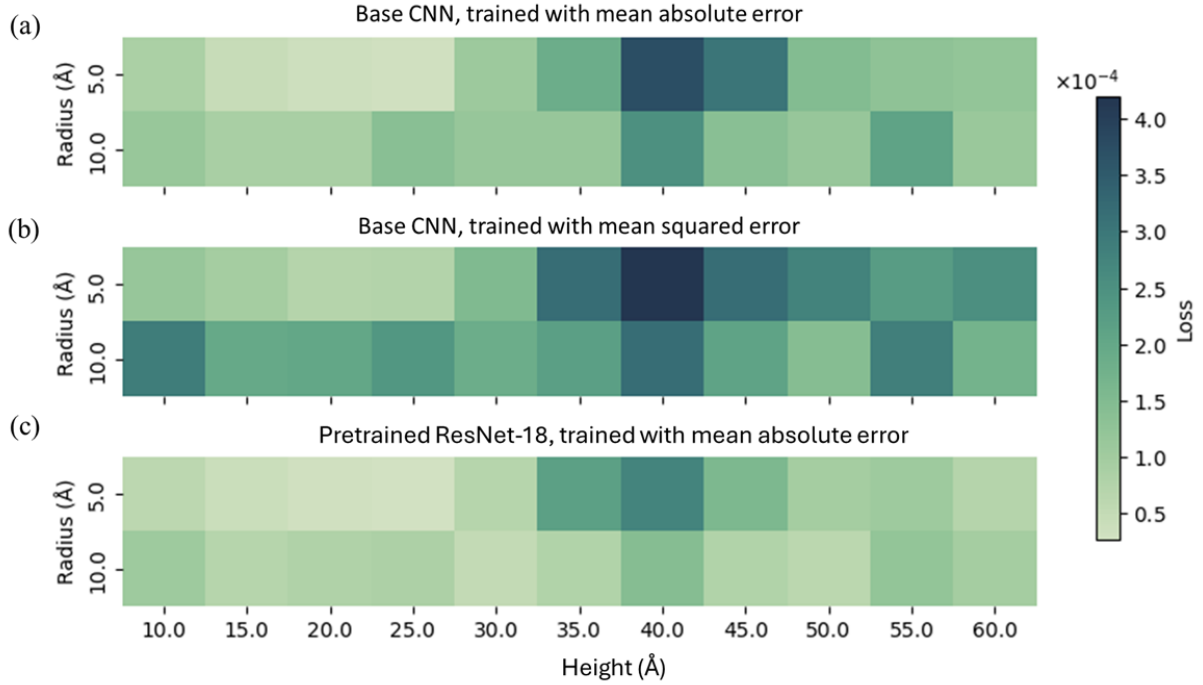


**Figure 7. Performance heatmap with respect to different cylindrical diffraction interaction volumes for (a) base CNN model trained with mean absolute error, (b) base CNN model trained with mean squared error, and (c) the pretrained ResNet-18 model trained with mean absolute error.**

The model was tested on virtual diffraction patterns not present in the training dataset to understand its ability to predict unseen configurations. Figure 8 predictions of SSRO along two strips in amorphous grain boundary complexion samples where Figure 8(a) comes from the grain boundary used for training, thus providing a baseline expectation for how well the model can perform, while Figure 8(b) is from another grain boundary not used for training. The predicted  $d_i$  profile of both seen and unseen images are in general consistent with the true values, especially in the ACTR. Minor deviation can be found in the crystalline and complexion interior regions. FCC regions associated with the grain interior were included in the training data to limited extent intentionally. These patterns can have artifacts due to cylinder sampling that can lead to unexpected overfitting and they are also simply less interesting because crystalline regions are easy to identify in experiments. In the complexion interior, the overall values predicted are

consistent with the true values, with minor errors found near the edges of the interior region. In general, the model exhibits generalizability considering the errors are small, as seen by the fact that all predictions are within the range expected for the respective regions in Figure 4(b). In addition, the  $d_i$  gradients in the ACTR are consistent with the true values in both profiles, demonstrating the model’s capability in the transition regions. The ACTRs have been identified as particularly important in past works. For example, after creating amorphous grain boundary complexions with MD/MC simulations, Garg and Rupert [65] found that the SSRO in the ACTRs can be predicted by the incompatibility between the confining grains, described by the grain boundary strain. The analysis tool presented here will enable complementary experimental studies of these features.

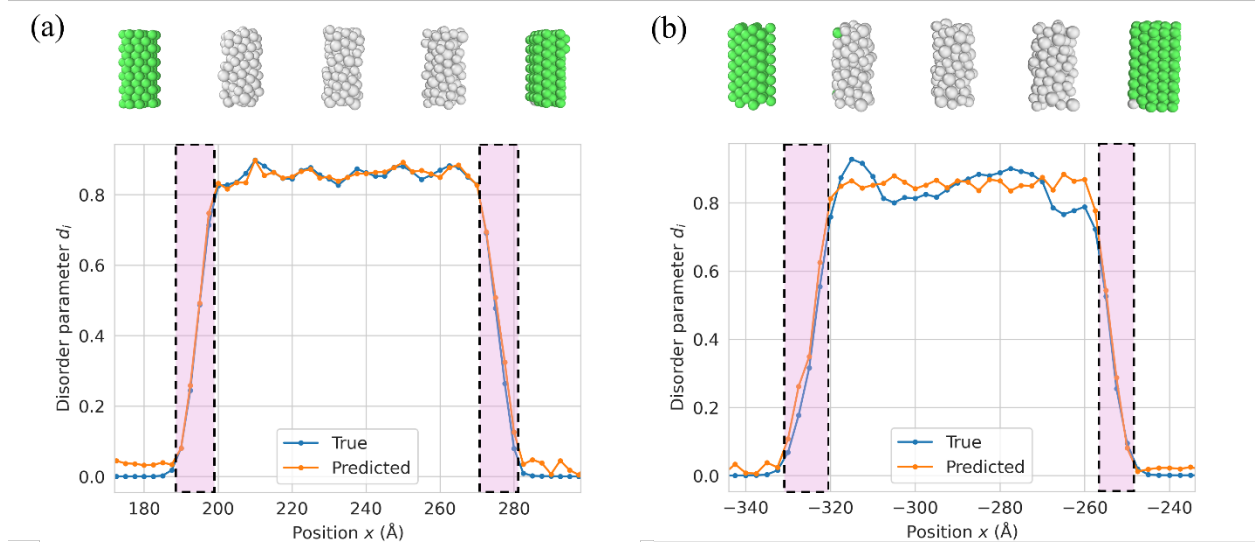
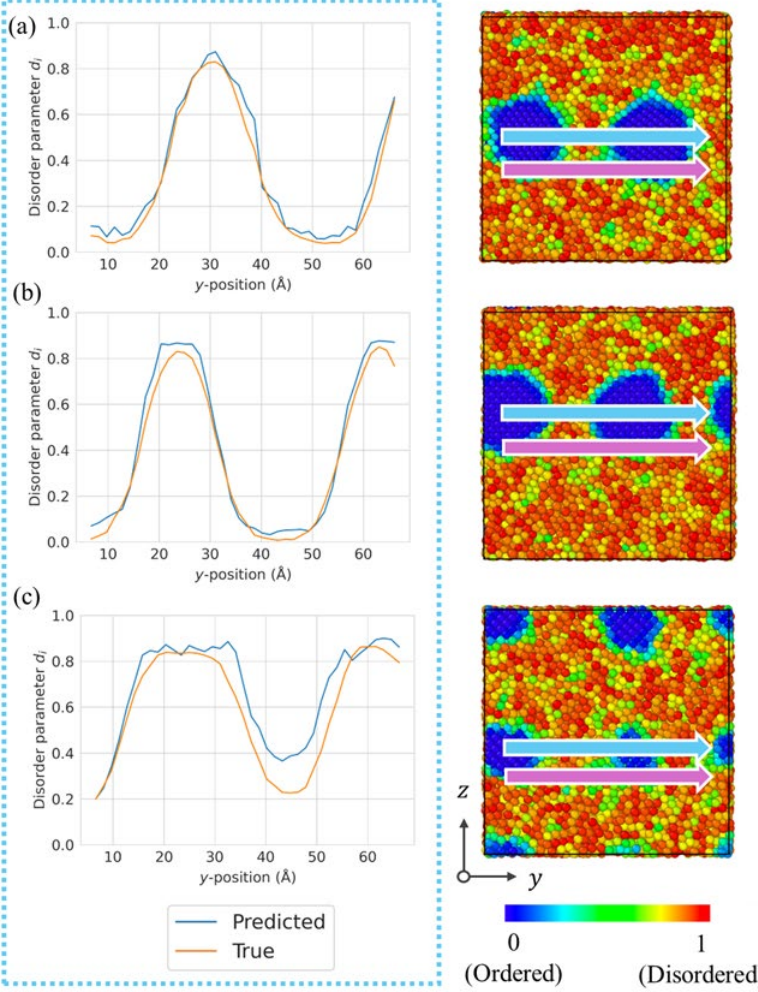


**Figure 8.** The predicted and true  $d_i$  profiles for virtual diffraction patterns take from profiles across amorphous complexions (a) used for training and (b) not used for training. The regions highlighted in pink correspond to the ACTRs.

To further test the usefulness of the model, virtual diffraction patterns from amorphous crystalline composites were tested. For these samples, the final nanocrystal diameters were  $\sim 2.5$  nm and  $\sim 1.7$  nm for the models that were created with initial radii of  $4\times$  and  $3\times$  the lattice parameter

of Cu. Figure 9 shows the predicted versus true disorder parameter from profiles taken across these samples, with one pathway crossing the embedded nanocrystals (Figures 9(a)-(c)) and another crossing the amorphous-amorphous interface in the composites (Figures 9(d)-(f)). The predictions generally closely align with the true  $d_i$  in all scans. When crossing the nanocrystals, the disorder parameter drops precipitously, although not exactly to zero. This is due to the regions sampled for virtual diffraction having a height of 20 Å, which exceeds the diameter of the nanocrystals. The effect is more obvious for the smaller nanocrystals in Figure 9(c). When moving across the amorphous-crystalline interfaces, disorder parameter drops as this feature is more ordered than the amorphous matrix, yet only reaches intermediate values. Disorder parameters that are similar to those measured in the ACTRs in Figure 4(b) are observed. The errors between predicted and true values generally are larger for the sample with smaller nanocrystals, likely due to the fact that interface curvature is more pronounced in these specimens. The ability to provide accurate descriptors of embedded nanocrystals and their interfaces in amorphous-crystalline composites is missing from experiments, yet has been a focus of computational work. For example, Brandl et al. [68] investigated these features in layered amorphous-crystalline composites with MD simulations, finding that significant distortion can occur which can stabilize and trap dislocations at the interfacial plane. The ability to quantify the structure of the amorphous-crystalline interfaces will also enrich combined computational experimental studies such as those pioneered by Abdelmawla et al. [69]

Across Nanocrystals



Across Amorphous-Crystalline Interfaces

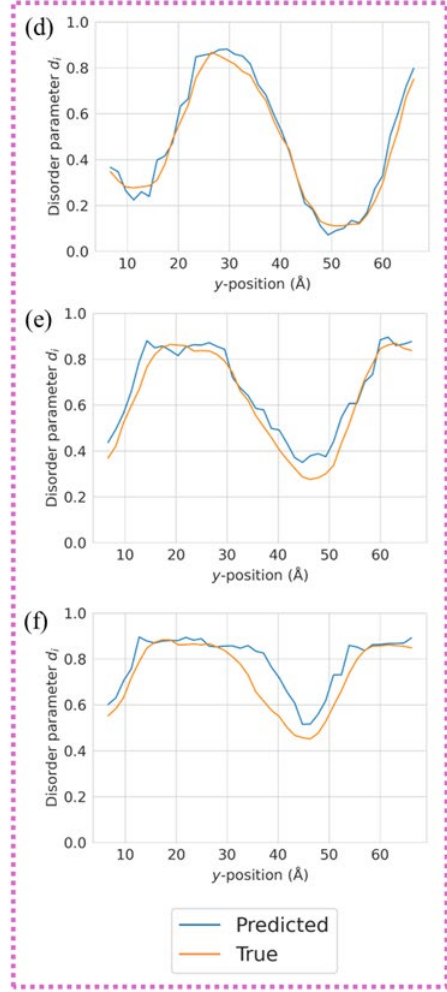


**Figure 9. Profiles of the predicted and true  $d_i$  for amorphous-crystalline composites containing nanocrystals of varying sizes: (a, d) radius of 4 lattice parameters with varied orientations, (b, e) radius of 4 lattice parameters with aligned orientations, and (c, f) radius of 3 lattice parameters with aligned orientations. The left column (a, b, c) shows scans passing through the nanocrystals, while the right column (d, e, f) shows scans passing through the amorphous-crystalline interface. Arrows indicate the positions of the profiles.**

To validate the model's ability to extract disorder parameter from experimental NBED images, the model was tested on published data on metallic glasses. Figure 10(a) representative images from the three datasets used here. The first two come from an arc melted Zr<sub>50</sub>Cu<sub>50</sub> metallic glass, where Islam et al. [70] were interested in the classification of medium-range order with different symmetries. As such, this data is subdivided into patterns with either 2-fold or 6-fold

symmetry. It is worth noting that the presence of symmetry does not necessarily mean a structure is ordered. For example, Hirata et al. [41] showed clear symmetries in distorted icosahedral packing motifs that were generally very disordered. The third dataset comes from a  $Zr_{50}Cu_{40}Al_{10}$  metallic glass that was investigated with NBED while being relaxed near its glass transition temperature by Nakazawa et al. [71]. Figure 10(b) presents the predicted disorder parameter for each dataset, with all predictions being relatively disordered and appropriate for a glassy structure. The values for the two  $Zr_{50}Cu_{50}$  sets are similar and have relatively high values, yet the mean values of the two predictions are distinguishable and differ by  $\sim 0.01$ . Icosahedral motifs have both 2- and 6-fold symmetries and thus a high value is reasonable. The  $Zr_{50}Cu_{40}Al_{10}$  sample that is undergoing relaxation has lower disorder parameters, consistent with the idea that the relaxation process allows the atomic structure to find more ordered configurations. Although there are only limited statistics in this dataset (six NBED patterns from three distinct times), longer relaxation times result in lower values of the disorder parameter. While the ground truths cannot be known here, it is promising that the values measured here (1) fall within the expected ranges for amorphous solids and (2) are distinguishable for different glasses, comparing the  $Zr_{50}Cu_{50}$  and  $Zr_{50}Cu_{40}Al_{10}$  alloys. Future investigations with NBED, particularly those involving known ground truths which display a gradient from ordered crystalline to disordered states, such amorphous grain boundary complexions, would greatly enhance model validation. In addition, it is important to note that the current model was only trained on Cu-Zr glasses structures and does not account for variations in the scattering factors among different atomic species. Thus, further research, such as the construction of a comprehensive database, is crucial for systems with substantial atomic size mismatches.

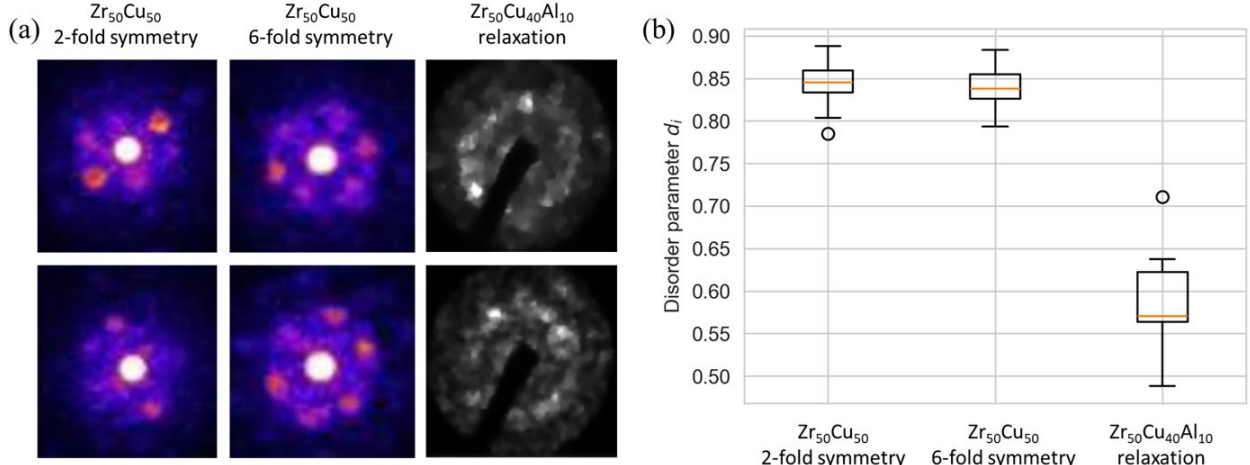


**Figure 10. NBED patterns from (a) a  $Cu_{50}Zr_{50}$  metallic glass with 2-fold and 6-fold symmetries, from Islam et. al [70] and reproduced with permission of Oxford University Press, and a  $Zr_{50}Cu_{40}Al_{10}$  undergoing relaxation near its glass transition temperature, from Nakazawa et. al [71] and reproduced with permission of Springer Nature. Images were denoised to allow for processing with our model. (b) Predicted disordered parameters from the three datasets, all being within reasonable values for an amorphous metal and with the sample undergoing relaxation exhibiting a less disordered structure.**

#### 4. Summary and Conclusions

An ML-driven analysis approach was created to quantify SSRO in amorphous solids using NBED and 4D-STEM data. By moving beyond analysis limited to discrete atomic motifs, our regression-based model uses the disorder parameter  $d_i$  to provide a continuous and interpretable metric of SSRO. Through transfer learning with ResNet-18, the model accurately predicts disorder parameter profiles using varied diffraction volume geometries, including cylinders and ellipsoids that compare favorably to experimental reality. In addition, the dependence on the geometry of the diffraction volume was probed to identify optimal combinations of radius and height, providing guidance for future experiments. The model was validated on unseen amorphous grain boundary complexions and amorphous-crystalline composite structure, with excellent agreement between predictions and true values, demonstrating that the framework is transferable. When applied to external experimental NBED datasets, the model correctly identified structural relaxation trends

and symmetry-related disorder levels, confirming its potential for experimental applications. Future research will focus on expanding the training database to include a broader range of alloy systems with diverse atomic size mismatches and scattering factors. The analysis framework developed here will enable experimental mapping of SSRO in amorphous solids, ultimately aiding in the rational design of amorphous alloys with tailored performance.

## **Data Availability**

Codes related to the model, data processing, and analysis used in this work are available in a GitHub repository at <https://github.com/NMMLab/nbed-ssro>.

## **Acknowledgements**

This research was supported by the U.S. Department of Energy, Office of Science, Basic Energy Sciences, under Award No. DE-SC0025195.

## References

- [1] H.W. Sheng, W.K. Luo, F.M. Alamgir, J.M. Bai, E. Ma, Atomic packing and short-to-medium-range order in metallic glasses, *Nature* 439 (2006) 419–425. <https://doi.org/10.1038/nature04421>.
- [2] W. Klement, R.H. Willens, P. Duwez, Non-crystalline Structure in Solidified Gold–Silicon Alloys, *Nature* 187 (1960) 869–870. <https://doi.org/10.1038/187869b0>.
- [3] Y.-K. Xu, H. Ma, J. Xu, E. Ma, Mg-based bulk metallic glass composites with plasticity and gigapascal strength, *Acta Materialia* 53 (2005) 1857–1866. <https://doi.org/10.1016/j.actamat.2004.12.036>.
- [4] J. Eckert, J. Das, K.B. Kim, F. Baier, M.B. Tang, W.H. Wang, Z.F. Zhang, High strength ductile Cu-base metallic glass, *Intermetallics* 14 (2006) 876–881. <https://doi.org/10.1016/j.intermet.2006.01.003>.
- [5] S. Pauly, J. Das, C. Duhamel, J. Eckert, Martensite Formation in a Ductile Cu47.5Zr47.5Al5 Bulk Metallic Glass Composite, *Advanced Engineering Materials* 9 (2007) 487–491. <https://doi.org/10.1002/adem.200700044>.
- [6] S. Pauly, G. Liu, G. Wang, U. Kühn, N. Mattern, J. Eckert, Microstructural heterogeneities governing the deformation of Cu47.5Zr47.5Al5 bulk metallic glass composites, *Acta Materialia* 57 (2009) 5445–5453. <https://doi.org/10.1016/j.actamat.2009.07.042>.
- [7] M. Ghidelli, A. Orekhov, A.L. Bassi, G. Terraneo, P. Djemia, G. Abadias, M. Nord, A. Béché, N. Gauquelin, J. Verbeeck, J.-P. Raskin, D. Schryvers, T. Pardoën, H. Idrissi, Novel class of nanostructured metallic glass films with superior and tunable mechanical properties, *Acta Materialia* 213 (2021) 116955. <https://doi.org/10.1016/j.actamat.2021.116955>.
- [8] Q. Wang, Y. Yang, H. Jiang, C.T. Liu, H.H. Ruan, J. Lu, Superior Tensile Ductility in Bulk Metallic Glass with Gradient Amorphous Structure, *Sci Rep* 4 (2014) 4757. <https://doi.org/10.1038/srep04757>.
- [9] L.-Q. Xing, Y. Li, K.T. Ramesh, J. Li, T.C. Hufnagel, Enhanced plastic strain in Zr-based bulk amorphous alloys, *Phys. Rev. B* 64 (2001) 180201. <https://doi.org/10.1103/PhysRevB.64.180201>.
- [10] M.M. Trexler, N.N. Thadhani, Mechanical properties of bulk metallic glasses, *Progress in Materials Science* 55 (2010) 759–839. <https://doi.org/10.1016/j.pmatsci.2010.04.002>.
- [11] L. Tian, Y.-Q. Cheng, Z.-W. Shan, J. Li, C.-C. Wang, X.-D. Han, J. Sun, E. Ma, Approaching the ideal elastic limit of metallic glasses, *Nat Commun* 3 (2012) 609. <https://doi.org/10.1038/ncomms1619>.
- [12] F.-F. Wu, K.C. Chan, S.-S. Jiang, S.-H. Chen, G. Wang, Bulk metallic glass composite with good tensile ductility, high strength and large elastic strain limit, *Sci Rep* 4 (2014) 5302. <https://doi.org/10.1038/srep05302>.
- [13] J. Xu, U. Ramamurty, E. Ma, The fracture toughness of bulk metallic glasses, *JOM* 62 (2010) 10–18. <https://doi.org/10.1007/s11837-010-0052-4>.
- [14] B. Gludovatz, S.E. Naleway, R.O. Ritchie, J.J. Kruzic, Size-dependent fracture toughness of bulk metallic glasses, *Acta Materialia* 70 (2014) 198–207. <https://doi.org/10.1016/j.actamat.2014.01.062>.
- [15] X. Rao, P.C. Si, J.N. Wang, Z. Xu, S. Xu, W.M. Wang, W.H. Wang, Preparation and mechanical properties of a new Zr–Al–Ti–Cu–Ni–Be bulk metallic glass, *Materials Letters* 50 (2001) 279–283. [https://doi.org/10.1016/S0167-577X\(01\)00240-3](https://doi.org/10.1016/S0167-577X(01)00240-3).

[16] J.J. Lewandowski, W.H. Wang, A.L. Greer, Intrinsic plasticity or brittleness of metallic glasses, *Philosophical Magazine Letters* 85 (2005) 77–87. <https://doi.org/10.1080/09500830500080474>.

[17] Z.F. Zhang, J. Eckert, L. Schultz, Difference in compressive and tensile fracture mechanisms of Zr59Cu20Al10Ni8Ti3 bulk metallic glass, *Acta Materialia* 51 (2003) 1167–1179. [https://doi.org/10.1016/S1359-6454\(02\)00521-9](https://doi.org/10.1016/S1359-6454(02)00521-9).

[18] Z.-Q. Song, Q. He, E. Ma, J. Xu, Fatigue endurance limit and crack growth behavior of a high-toughness Zr61Ti2Cu25Al12 bulk metallic glass, *Acta Materialia* 99 (2015) 165–175. <https://doi.org/10.1016/j.actamat.2015.07.071>.

[19] J. Ding, Y.-Q. Cheng, E. Ma, Full icosahedra dominate local order in Cu64Zr34 metallic glass and supercooled liquid, *Acta Materialia* 69 (2014) 343–354. <https://doi.org/10.1016/j.actamat.2014.02.005>.

[20] M.H. Yang, J.H. Li, B.X. Liu, Proposed correlation of structure network inherited from producing techniques and deformation behavior for Ni-Ti-Mo metallic glasses via atomistic simulations, *Sci Rep* 6 (2016) 29722. <https://doi.org/10.1038/srep29722>.

[21] Y.L. Sun, J. Shen, Icosahedral ordering in Cu60Zr40 metallic glass: Molecular dynamics simulations, *Journal of Non-Crystalline Solids* 355 (2009) 1557–1560. <https://doi.org/10.1016/j.jnoncrysol.2009.06.010>.

[22] Y.Q. Cheng, H.W. Sheng, E. Ma, Relationship between structure, dynamics, and mechanical properties in metallic glass-forming alloys, *Phys. Rev. B* 78 (2008) 014207. <https://doi.org/10.1103/PhysRevB.78.014207>.

[23] T. Egami, V. Vitek, Local structural fluctuations and defects in metallic glasses, *Journal of Non-Crystalline Solids* 61–62 (1984) 499–510. [https://doi.org/10.1016/0022-3093\(84\)90596-9](https://doi.org/10.1016/0022-3093(84)90596-9).

[24] J. Ding, S. Patinet, M.L. Falk, Y. Cheng, E. Ma, Soft spots and their structural signature in a metallic glass, *Proceedings of the National Academy of Sciences* 111 (2014) 14052–14056. <https://doi.org/10.1073/pnas.1412095111>.

[25] A.J. Cao, Y.Q. Cheng, E. Ma, Structural processes that initiate shear localization in metallic glass, *Acta Materialia* 57 (2009) 5146–5155. <https://doi.org/10.1016/j.actamat.2009.07.016>.

[26] M.Q. Jiang, L.H. Dai, Shear-band toughness of bulk metallic glasses, *Acta Materialia* 59 (2011) 4525–4537. <https://doi.org/10.1016/j.actamat.2011.03.075>.

[27] B.S. Shang, M.Z. Li, Y.G. Yao, Y.J. Lu, W.H. Wang, Evolution of atomic rearrangements in deformation in metallic glasses, *Phys. Rev. E* 90 (2014) 042303. <https://doi.org/10.1103/PhysRevE.90.042303>.

[28] J.L. Wardini, C.M. Grigorian, T.J. Rupert, Amorphous complexions alter the tensile failure of nanocrystalline Cu-Zr alloys, *Materialia* 17 (2021) 101134. <https://doi.org/10.1016/j.mtla.2021.101134>.

[29] A. Khalajhedayati, Z. Pan, T.J. Rupert, Manipulating the interfacial structure of nanomaterials to achieve a unique combination of strength and ductility, *Nat Commun* 7 (2016) 10802. <https://doi.org/10.1038/ncomms10802>.

[30] G. Wu, C. Liu, L. Sun, Q. Wang, B. Sun, B. Han, J.-J. Kai, J. Luan, C.T. Liu, K. Cao, Y. Lu, L. Cheng, J. Lu, Hierarchical nanostructured aluminum alloy with ultrahigh strength and large plasticity, *Nat Commun* 10 (2019) 5099. <https://doi.org/10.1038/s41467-019-13087-4>.

[31] G. Wu, S. Balachandran, B. Gault, W. Xia, C. Liu, Z. Rao, Y. Wei, S. Liu, J. Lu, M. Herbig, W. Lu, G. Dehm, Z. Li, D. Raabe, Crystal–Glass High-Entropy Nanocomposites with Near

Theoretical Compressive Strength and Large Deformability, (n.d.). <https://doi.org/10.1002/adma.202002619>.

[32] J. Ding, D. Neffati, Q. Li, R. Su, J. Li, S. Xue, Z. Shang, Y. Zhang, H. Wang, Y. Kulkarni, X. Zhang, Thick grain boundary induced strengthening in nanocrystalline Ni alloy, *Nanoscale* 11 (2019) 23449–23458. <https://doi.org/10.1039/C9NR06843K>.

[33] Z. Pan, T.J. Rupert, Amorphous intergranular films as toughening structural features, *Acta Materialia* 89 (2015) 205–214. <https://doi.org/10.1016/j.actamat.2015.02.012>.

[34] P. Garg, T.J. Rupert, Local structural ordering determines the mechanical damage tolerance of amorphous grain boundary complexions, *Scripta Materialia* 237 (2023) 115712. <https://doi.org/10.1016/j.scriptamat.2023.115712>.

[35] D. Aksoy, P. Cao, J.R. Trelewicz, J.P. Wharry, T.J. Rupert, Enhanced Radiation Damage Tolerance of Amorphous Interphase and Grain Boundary Complexions in Cu-Ta, *JOM* 76 (2024) 2870–2883. <https://doi.org/10.1007/s11837-024-06382-z>.

[36] X. Pan, W.D. Kaplan, M. Rühle, R.E. Newnham, Quantitative Comparison of Transmission Electron Microscopy Techniques for the Study of Localized Ordering on a Nanoscale, *Journal of the American Ceramic Society* 81 (1998) 597–605. <https://doi.org/10.1111/j.1151-2916.1998.tb02379.x>.

[37] S. Hata, S. Matsumura, N. Kuwano, K. Oki, D. Shindo, Short range order in Ni<sub>4</sub>Mo and its high resolution electron microscope images, *Acta Materialia* 46 (1998) 4955–4961. [https://doi.org/10.1016/S1359-6454\(98\)00180-3](https://doi.org/10.1016/S1359-6454(98)00180-3).

[38] S. Hata, T. Mitate, N. Kuwano, S. Matsumura, D. Shindo, K. Oki, Short range order structures in fcc-based Ni–Mo studied by high resolution transmission electron microscopy with image processing, *Materials Science and Engineering: A* 312 (2001) 160–167. [https://doi.org/10.1016/S0921-5093\(00\)01872-4](https://doi.org/10.1016/S0921-5093(00)01872-4).

[39] A. Hirata, S. Tokuda, C. Nakajima, S. Zha, Local structural modelling and local pair distribution function analysis for Zr–Pt metallic glass, *Sci Rep* 14 (2024) 13322. <https://doi.org/10.1038/s41598-024-64380-2>.

[40] A. Hirata, P. Guan, T. Fujita, Y. Hirotsu, A. Inoue, A.R. Yavari, T. Sakurai, M. Chen, Direct observation of local atomic order in a metallic glass, *Nature Mater* 10 (2011) 28–33. <https://doi.org/10.1038/nmat2897>.

[41] A. Hirata, L.J. Kang, T. Fujita, B. Klumov, K. Matsue, M. Kotani, A.R. Yavari, M.W. Chen, Geometric Frustration of Icosahedron in Metallic Glasses, *Science* 341 (2013) 376–379. <https://doi.org/10.1126/science.1232450>.

[42] C. Ophus, Four-Dimensional Scanning Transmission Electron Microscopy (4D-STEM): From Scanning Nanodiffraction to Ptychography and Beyond, *Microsc Microanal* 25 (2019) 563–582. <https://doi.org/10.1017/S1431927619000497>.

[43] C. Shi, M.C. Cao, S.M. Rehn, S.-H. Bae, J. Kim, M.R. Jones, D.A. Muller, Y. Han, Uncovering material deformations via machine learning combined with four-dimensional scanning transmission electron microscopy, *Npj Comput Mater* 8 (2022) 114. <https://doi.org/10.1038/s41524-022-00793-9>.

[44] S. Hwang, H. Koh, J.C. Yang, Electron Microscopy Approaches to Unraveling the Structure of Amorphous Materials, *Small Methods* n/a (n.d.) e01852. <https://doi.org/10.1002/smtd.202501852>.

[45] J. Zimmermann, B. Langbehn, R. Cucini, M. Di Fraia, P. Finetti, A.C. LaForge, T. Nishiyama, Y. Ovcharenko, P. Piseri, O. Plekan, K.C. Prince, F. Stienkemeier, K. Ueda, C. Callegari, T.

Möller, D. Rupp, Deep neural networks for classifying complex features in diffraction images, *Phys. Rev. E* 99 (2019) 063309. <https://doi.org/10.1103/PhysRevE.99.063309>.

[46] L.C.O. Tiong, J. Kim, S.S. Han, D. Kim, Identification of crystal symmetry from noisy diffraction patterns by a shape analysis and deep learning, *Npj Comput Mater* 6 (2020) 196. <https://doi.org/10.1038/s41524-020-00466-5>.

[47] S. Kang, V. Wollersen, C. Minnert, K. Durst, H.-S. Kim, C. Kübel, X. Mu, Mapping local atomic structure of metallic glasses using machine learning aided 4D-STEM, *Acta Materialia* 263 (2024) 119495. <https://doi.org/10.1016/j.actamat.2023.119495>.

[48] A. Bruefach, C. Ophus, M.C. Scott, Analysis of Interpretable Data Representations for 4D-STEM Using Unsupervised Learning, *Microanal* 28 (2022) 1998–2008. <https://doi.org/10.1017/S1431927622012259>.

[49] P.J. Steinhardt, D.R. Nelson, M. Ronchetti, Bond-orientational order in liquids and glasses, *Phys. Rev. B* 28 (1983) 784–805. <https://doi.org/10.1103/PhysRevB.28.784>.

[50] A.P. Thompson, H.M. Aktulga, R. Berger, D.S. Bolintineanu, W.M. Brown, P.S. Crozier, P.J. in 't Veld, A. Kohlmeyer, S.G. Moore, T.D. Nguyen, R. Shan, M.J. Stevens, J. Tranchida, C. Trott, S.J. Plimpton, LAMMPS - a flexible simulation tool for particle-based materials modeling at the atomic, meso, and continuum scales, *Computer Physics Communications* 271 (2022) 108171. <https://doi.org/10.1016/j.cpc.2021.108171>.

[51] M.I. Mendelev, Y. Sun, F. Zhang, C.Z. Wang, K.M. Ho, Development of a semi-empirical potential suitable for molecular dynamics simulation of vitrification in Cu-Zr alloys, *The Journal of Chemical Physics* 151 (2019) 214502. <https://doi.org/10.1063/1.5131500>.

[52] Z. Pan, T.J. Rupert, Spatial variation of short-range order in amorphous intergranular complexions, *Computational Materials Science* 131 (2017) 62–68. <https://doi.org/10.1016/j.commatsci.2017.01.033>.

[53] A. Stukowski, Visualization and analysis of atomistic simulation data with OVITO—the Open Visualization Tool, *Modelling Simul. Mater. Sci. Eng.* 18 (2009) 015012. <https://doi.org/10.1088/0965-0393/18/1/015012>.

[54] V.A. Borodin, Local atomic arrangements in polytetrahedral materials, *Philosophical Magazine A* 79 (1999) 1887–1907. <https://doi.org/10.1080/01418619908210398>.

[55] A.L.-S. Chua, N.A. Benedek, L. Chen, M.W. Finn, A.P. Sutton, A genetic algorithm for predicting the structures of interfaces in multicomponent systems, *Nature Mater* 9 (2010) 418–422. <https://doi.org/10.1038/nmat2712>.

[56] S. von Alftan, P.D. Haynes, K. Kaski, A.P. Sutton, Are the Structures of Twist Grain Boundaries in Silicon Ordered at 0 K?, *Phys. Rev. Lett.* 96 (2006) 055505. <https://doi.org/10.1103/PhysRevLett.96.055505>.

[57] K. He, X. Zhang, S. Ren, J. Sun, Deep Residual Learning for Image Recognition, (2015). <https://doi.org/10.48550/arXiv.1512.03385>.

[58] D.P. Kingma, J. Ba, Adam: A Method for Stochastic Optimization, (2017). <https://doi.org/10.48550/arXiv.1412.6980>.

[59] T. Fukunaga, K. Itoh, T. Otomo, K. Mori, M. Sugiyama, H. Kato, M. Hasegawa, A. Hirata, Y. Hirotsu, A.C. Hannon, Voronoi analysis of the structure of Cu–Zr and Ni–Zr metallic glasses, *Intermetallics* 14 (2006) 893–897. <https://doi.org/10.1016/j.intermet.2006.01.006>.

[60] L. Huang, C.Z. Wang, S.G. Hao, M.J. Kramer, K.M. Ho, Short- and medium-range order in amorphous Zr<sub>2</sub>Ni metallic alloy, *Phys. Rev. B* 81 (2010) 094118. <https://doi.org/10.1103/PhysRevB.81.094118>.

- [61] S. Trady, M. Mazroui, A. Hasnaoui, K. Saadouni, Molecular dynamics study of atomic-level structure in monatomic metallic glass, *Journal of Non-Crystalline Solids* 443 (2016) 136–142. <https://doi.org/10.1016/j.jnoncrysol.2016.04.004>.
- [62] M. Kbirou, S. Trady, A. Hasnaoui, M. Mazroui, Short and medium-range orders in Co<sub>3</sub>Al metallic glass, *Chemical Physics* 513 (2018) 58–66. <https://doi.org/10.1016/j.chemphys.2018.06.018>.
- [63] L. Ward, D. Miracle, W. Windl, O.N. Senkov, K. Flores, Structural evolution and kinetics in Cu-Zr metallic liquids from molecular dynamics simulations, *Phys. Rev. B* 88 (2013) 134205. <https://doi.org/10.1103/PhysRevB.88.134205>.
- [64] W.P. Weeks, K.M. Flores, Structural building-blocks of disordered Cu-Zr alloys, *Acta Materialia* 265 (2024) 119624. <https://doi.org/10.1016/j.actamat.2023.119624>.
- [65] P. Garg, T.J. Rupert, Grain incompatibility determines the local structure of amorphous grain boundary complexions, *Acta Materialia* 244 (2023) 118599. <https://doi.org/10.1016/j.actamat.2022.118599>.
- [66] E. Ma, Tuning order in disorder, *Nature Mater.* 14 (2015) 547–552. <https://doi.org/10.1038/nmat4300>.
- [67] C.C. Wang, K.J. Dong, A.B. Yu, Analysis of Voronoi clusters in the packing of uniform spheres, in: Sydney, Australia, 2013: pp. 353–356. <https://doi.org/10.1063/1.4811940>.
- [68] C. Brandl, T.C. Germann, A. Misra, Structure and shear deformation of metallic crystalline–amorphous interfaces, *Acta Materialia* 61 (2013) 3600–3611. <https://doi.org/10.1016/j.actamat.2013.02.047>.
- [69] A. Abdelmawla, T. Phan, L. Xiong, A. Bastawros, A combined experimental and computational analysis on how material interface mediates plastic flow in amorphous/crystalline composites, *Journal of Materials Research* 36 (2021) 2816–2829. <https://doi.org/10.1557/s43578-021-00269-4>.
- [70] M. Islam, S.-C. Lee, H.-S. Chung, J. Hwang, Revealing Medium Range Ordering in Zr-based Metallic Glasses Using Machine Learning Analysis of 4D-STEM Nanodiffraction, *Microanal* 31 (2025) ozaf048.798. <https://doi.org/10.1093/mam/ozaf048.798>.
- [71] K. Nakazawa, K. Mitsuishi, K. Iakoubovskii, S. Kohara, K. Tsuchiya, Structure-dynamics relation in metallic glass revealed by 5-dimensional scanning transmission electron microscopy, *NPG Asia Mater* 16 (2024) 57. <https://doi.org/10.1038/s41427-024-00577-1>.